Clément Michoud · Dario Carrea · Stéphane Costa · Marc-Henri Derron · Michel Jaboyedoff · Christophe Delacourt · Olivier Maquaire · Pauline Letortu · Robert Davidson

Landslide detection and monitoring capability of boat-based mobile laser scanning along Dieppe coastal cliffs, Normandy

Abstract Integrated in a wide research assessing destabilizing and triggering factors to model cliff dynamic along the Dieppe's shoreline in High Normandy, this study aims at testing boat-based mobile LiDAR capabilities by scanning 3D point clouds of the unstable coastal cliffs. Two acquisition campaigns were performed in September 2012 and September 2013, scanning (1) a 30-km-long shoreline and (2) the same test cliffs in different environmental conditions and device settings. The potentials of collected data for 3D modelling, change detection and landslide monitoring were afterward assessed. By scanning during favourable meteorological and marine conditions and close to the coast, mobile LiDAR devices are able to quickly scan a long shoreline with median point spacing up to 10cm. The acquired data are then sufficiently detailed to map geomorphological features smaller than 0.5m². Furthermore, our capability to detect rockfalls and erosion deposits (>m³) is confirmed, since using the classical approach of computing differences between sequential acquisitions reveals many cliff collapses between Pourville and Quiberville and only sparse changes between Dieppe and Belleville-sur-Mer. These different change rates result from different rockfall susceptibilities. Finally, we also confirmed the capability of the boat-based mobile LiDAR technique to monitor single large changes, characterizing the Dieppe landslide geometry with two main active scarps, retrogression up to 40m and about 100,000m³ of eroded materials.

Keywords Mobile laser scanning · Coastline change detection · Rockfall · Landslide monitoring · High Normandy coastal cliffs

Introduction

Laser scanning and 3D point clouds have changed our perception and interpretation of slope deformations for the last 15 years and are nowadays widely used for landslide monitoring and warning systems (as reviewed by the SafeLand deliverable 4.1 2012; Jaboyedoff et al. 2012; Baroň and Supper 2013; Michoud et al. 2013). Terrestrial Laser scanning (TLS, terrestrial LiDAR) indeed allows measuring topography with very high point density, including inaccessible steep slopes. 3D displacements of rock masses can also be extracted by detecting topographic changes on sequential TLS acquisitions, as reviewed by Abellán et al. (2014); TLS-based rockfall detections were also carried out for detailed investigations on confined coastal cliffs (e.g. in Lim et al. 2005; Rosser et al. 2005 and Rosser et al. 2007; Collins and Sitar 2008; Young et al. 2013; Letortu et al. 2014). However, this technique turned out not to be optimized for stability assessments over kilometre-long shorelines: accurate (and therefore time-consuming) acquisitions along large areas are indeed not likely during short low tide periods and require in addition tedious post-processing to align the numerous scans. Despite being able to scan very large areas in a short time, aerial laser scanning devices (ALS) are also not indicated to detect rockfalls on the front of vertical coastal cliffs (Young et al. 2013) since they would not record dense and accurate backscattered pulses on cliffs due to the high incidence angle between the latter and the laser beam (Baltsavias 1999; Lichti et al. 2005). Alternatively, mobile laser scanning (MLS) devices (Jaakkola et al. 2008; Kukko et al. 2012; Glennie et al. 2013) can be mounted on boats, setting up the scanner horizontally with a frontal view on shores (Fig. 1); they have indeed recently demonstrated their capability to map topographic changes along fluvial banks (Alho et al. 2009; Vaaja et al. 2011, 2013).

A wide research plan intends to assess landslide destabilizing and triggering factors and to model the cliff dynamic of the French High Normandy coasts (Letortu 2013; Letortu et al. 2014). The total length of the High Normandy cliffs is around 110 km with an average height of 60 m. Within this framework, this detailed study aims at testing MLS capabilities in tossing water of the Channel sea. The Dieppe cliffs are mainly formed by sub-horizontal deposits of soft Cretaceous chalk interlayered by thin bands of biogenic flint (Fig. 2) corresponding to the western termination of the Paris Basin. Due to their particularly low mechanical strength and being directly hit by oceanic storms (Costa et al. 2004 and Costa 2014; Letortu et al. 2012, 2014), the high cliffs are thus destabilized by an intense weathering and sea erosion. Rockfalls are therefore regularly observed (e.g. in Costa 1997 and Costa 2014; Duperret et al. 2002; Dewez et al. 2013) and contribute to quick retrogressive cliff processes of about 20 cm/year on average (Costa et al. 2004).

By acquiring dense 3D point clouds along vertical coastal cliffs and intertidal areas in September 2012, we want indeed to assess (a) the median point spacing for different acquisition conditions and (b) the repeatability of point clouds of the same area acquired several times. In addition, after a second acquisition campaign held in September 2013, we also aim at estimating the MLS capability to assess retreat rates over kilometre-long coastal cliffs, based on rockfall events and cliff foot erosion detection and quantification using classic shortest distance comparison approaches. All acronyms used in this note are summarized in Table 1.

Mobile laser scanning principles

Terrestrial laser scanning (TLS) is an active optical sensor which allows providing *xyz* point clouds of the topography with a high
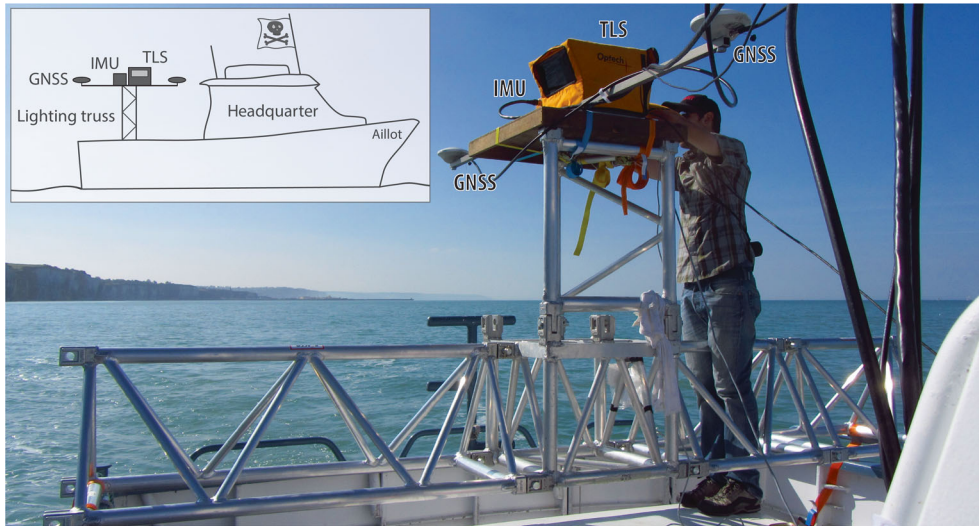
Fig. 1 MLS setup on the boat L'Aillot. The system is tied up on the lighting truss at the same elevation as the cabin, in order to ensure a good GNSS horizon for the antennas and to avoid splash on the MLS

resolution (Beraldin et al. 2000; Gordon et al. 2001). All long-range TLS devices use laser pulses and are based on the the time-of-flight (TOF) principle (Vosselman and Maas 2010). The sensor indeed emits laser pulses on a line of sight (LOS) perfectly known relatively to the device; the direction of the laser is controlled by one or two internal mirrors reflecting the signal and/or motors orienting the device itself. Emitted pulses are back-scattered by the terrain, vegetation, particles as sea spray and air dust, etc. The TOF that the pulses take to go forth and back is recorded and is then converted into the range, knowing the light velocity (Eq. 1):

$$r = \frac{1}{2} \cdot c \cdot \Delta t \qquad (1)$$

where r is the range from the sensor to the target [in m], c is the light velocity in air [in m/s], and Δt is the TOF [in s].

A 3D image of the topography can thus be created from the recorded LOS and TOF. Now, when performing scans from moving platforms such as boats, the directions of emitted pulses are only known relatively to the device, but the position and orientation of the device are changing during the acquisitions, which prevent from having all the points in the same local reference system.

However, by adding to the LiDAR an inertial navigation system (INS), composed of two global navigation satellite system (GNSS) antennas and an inertial measurement unit (IMU), it is then possible to achieve surveys from a vessel. The IMU indeed records the attitude of the platform on the boat by continuously measuring the Cardan angles (Fig. 3), i.e. (α) yaw (or heading, azimuth of direction of motion), (β) pitch (back and forth shake) and (γ) roll (left-to-right shake). The GNSS antennas furthermore localize the instrument and

Fig. 2 Location and illustration of classic morphology of vertical coastal cliffs close to Dieppe, French Normandy

Table 1 Table of main acronyms used in this note

| Acronym	Definition
α, β, γ	Yaw, pitch and roll of the Cardan angles
ALS	Aerial laser scanning
Bft	Beaufort scale, describing marine conditions (wind, swell height, etc.)
GAMS	GPS Azimuth Measurement Subsystem™
GIS	Geographic information system
GNSS	Global navigation satellite system
ICP	Iterative closest point
IGN	Institut national de l'information géographique et forestière
IMU	Inertial measurement unit
INS	Inertial navigation system
Jn	Point clouds acquired on 20 September 2012
Jn'	Point clouds acquired on 26 September 2013
LiDAR	Light detection and ranging
LOS	Line of sight
MLS	Mobile laser scanning
Mn'	Point clouds acquired on 25 September 2013
SBET	Smoothed best estimate of trajectory
TLS	Terrestrial laser scanning
TOF	Time of flight
UTM	Universal transverse Mercator
WGS	World geodetic system
xyzi file	ASCII text file structured in 4 columns: *x*, *y*, *z* coordinates and signal intensity
xyzid file	ASCII text file structured in 5 columns: as *xyzi*, plus point-to-surface difference
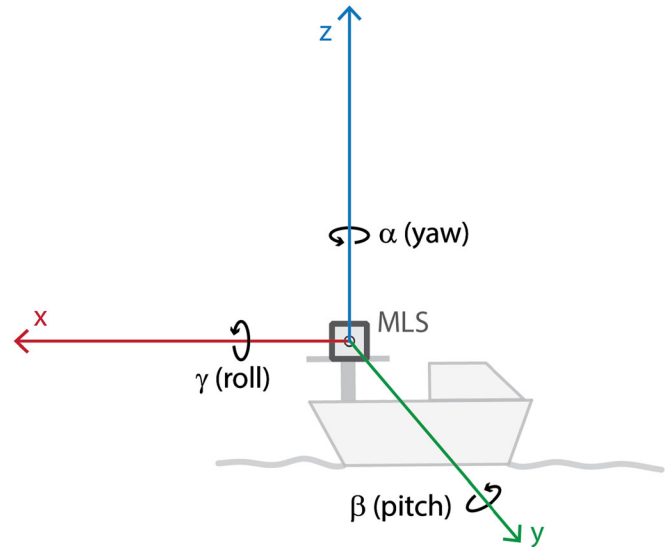
Fig. 3 Illustration of the Cardan angles, i.e. yaw, pitch and roll

enhance the yaw measurement. In order to reconstruct the 3D topography, the entire point cloud is then post-processed, performing for each single point a rigid body transformation; we can indeed apply to each point a roto-translation matrix (Eq. 2) to transform coordinates from its LiDAR internal system to a georeferenced system (Tupling and Pierrynowski 1987; Lichti et al. 2002; Oppikofer et al. 2009).

$$\begin{pmatrix} p_x \\ p_y \\ p_z \\ 1 \end{pmatrix} = (R + T) \times \begin{pmatrix} l_x \\ l_y \\ l_z \\ 1 \end{pmatrix} \tag{2}$$

with

$$R = R_z(\alpha) \times R_y(\beta) \times R_x(\gamma) = \begin{pmatrix} \cos(\alpha) & -\sin(\alpha) & 0 & 0 \\ \sin(\alpha) & \cos(\alpha) & 0 & 0 \\ 0 & 0 & 1 & 0 \\ 0 & 0 & 0 & 0 \end{pmatrix} \times \begin{pmatrix} \cos(\beta) & 0 & \sin(\beta) & 0 \\ 0 & 1 & 0 & 0 \\ -\sin(\beta) & 0 & \cos(\beta) & 0 \\ 0 & 0 & 0 & 0 \end{pmatrix} \times \begin{pmatrix} 1 & 0 & 0 & 0 \\ 0 & \cos(\gamma) & -\sin(\gamma) & 0 \\ 0 & \sin(\gamma) & \cos(\gamma) & 0 \\ 0 & 0 & 0 & 0 \end{pmatrix}$$

$$\text{and } T = \begin{pmatrix} 0 & 0 & 0 & t_x \\ 0 & 0 & 0 & t_y \\ 0 & 0 & 0 & t_z \\ 0 & 0 & 0 & 1 \end{pmatrix} \Rightarrow R + T = \begin{pmatrix} \cos(\alpha)\cdot\cos(\beta) & \cos(\alpha)\cdot\sin(\beta)\cdot\sin(\gamma)-\sin(\alpha)\cdot\cos(\gamma) & \cos(\alpha)\cdot\sin(\beta)\cdot\cos(\gamma)+\sin(\alpha)\cdot\sin(\gamma) & t_x \\ \sin(\alpha)\cdot\cos(\beta) & \sin(\alpha)\cdot\sin(\beta)\cdot\sin(\gamma)+\cos(\alpha)\cdot\cos(\gamma) & \sin(\alpha)\cdot\sin(\beta)\cdot\cos(\gamma)-\cos(\alpha)\cdot\sin(\gamma) & t_y \\ -\sin(\beta) & \cos(\beta)\cdot\sin(\gamma) & \cos(\beta)\cdot\cos(\gamma) & t_z \\ 0 & 0 & 0 & 1 \end{pmatrix}$$

where

- R is the total rotation matrix; R_x, R_y and R_z are the fundamental rotation matrix about resp. axes *x*, *y* and *z*.
- T is the translation matrix.
- α, β and γ are resp. the yaw, pitch and roll of the Cardan angles [in °], measured by the IMU.
- $(p_x p_y p_z)$ are the point coordinates [in m] georeferenced in the UTM system.

- $(t_x t_y t_z)$ are the LiDAR location coordinates [in m] in the UTM system, measured by the GNSS.
- $(l_x l_y l_z)$ are the point coordinates [in m] in the LiDAR internal system, measured by the laser sensor.

MLS and ALS techniques are based on the same principles (Vosselman and Maas 2010). Nevertheless, MLS devices are smaller, lighter and cheaper than ALS ones; they are

furthermore able to scan the coastline from a direct and horizontal point of view, ensuring a high point cloud density even on sub-vertical cliffs (cf. "Mobile laser scanning data" section).

Exhaustive reviews of mobile and terrestrial LiDAR principles and applications are available in Vosselman and Maas (2010), Jaboyedoff et al. (2012), Kukko et al. (2012), Williams et al. (2013) and Abellán et al. (2014).

Point cloud processing

Devices' technical specifications
The INS used for this study is an Applanix™ POS MV 320-V4, having the following features according to its manufacturer:

– Acquisition frequency—1 Hz
– Angular accuracy—0.020°, up to 0.010° with a GNSS base station
– Positioning accuracy—up to 0.02 m, corrected with a GNSS base station

In addition to the INS, we used a Laser Scanner Optech™ Ilris Long Range, having the following features according to its manufacturer:

– Laser wavelength—1064 nm
– Pulse rate—10 kHz
– Maximum range—about 2000 m at 20 % reflectivity
– Mean precision of range estimation—4 mm at 100 m
– Angular accuracy—8 mm at 100 m
– Beam diameter—125 mm at 500 m (according to Baltsavias 1999, beam diameter is approx. equal to beam divergence, here 250 μrad, times range)

For this study, an internal mirror of the LiDAR device is set up to move the laser beam only along vertical predefined LOS; the vessel attitude, and especially its velocity, is therefore mainly controlling the distance between successive scanned lines. The influence of the LiDAR device setup and the boat attitude

is hereafter considered in the "MLS point clouds capability assessment" section.

Acquisitions on the vessel

Setup and calibration on the vessel
As illustrated in Fig. 1, the IMU and the TLS of the mobile system are first screwed on an aluminium plate and the GNSS antennas are fixed on two arms of about 2 m length at each side of the plate. The *xyz* vector components from the IMU to the master GNSS antennas and to the laser scanner are then measured with a subcentimetric precision, according to target located on the top of the IMU box. These measures are valid as long as we set up the MLS system on the same plate.

For both campaigns, the MLS plate is then firmly tied up on a lighting truss on the back deck of the fishing boat L'Aillot. The system is set up as high as possible to avoid splash on the LiDAR device, since it is not waterproof, and to ensure a consistent GNSS horizon for the antenna close to the cabin (usually signals from seven to nine GNSS satellites are caught, cf. Tables 2 and 3).

The GPS Azimuth Measurement Subsystem™ (GAMS) has afterward to be calibrated in order to enhance yaw and location measurements. By doing loops or 8-shaped trajectories during about 10 min, the INS is able to fix the phase ambiguity of GNSS signals recorded by the two antennas and to calculate with a millimetric precision the vector between the two GNSS antennas (Applanix 2011). This calibration is performed every day.

Description of acquisitions
After several tests realized the days before, four operational acquisitions, named Jn, have been performed on 20 September 2012 on the Ailly and Puys sites, during a sunny day with a calm sea (2 Bft). Puys cliffs have been scanned once, whereas the Cap d'Ailly shoreline has been acquired three times with large overlaps, to test point spacing and repeatability under different conditions, mainly changing the boat speed, range to the cliffs and LiDAR angular apertures and resolutions.

Table 2 Conditions and LiDAR acquisition parameters of the four scans realized on 20 September 2012

	J1	J2	J3	J4
Sector	Ailly	Ailly>Dieppe	Ailly	Puys
Scan beginning time	11h28	12h28	15h21	16h16
Scan end time	11h48	13h13	15h36	16h55
Acquisition length	2500 m	5700 m	1000 m	3400 m
Range to cliffs	~650 m	~350–500 m	~200 m	~300 m
Tide	Low	Low	High	High
Boat velocity	~4 kn	~4 kn	~2.2 kn	~3.3 kn
Sea conditions (Beaufort)	2 Bft	2 Bft	2 Bft	2 Bft
Sun	From the side	From the side	In front	From the side
LiDAR vertical aperture	14°	14°	23°	18°
Angular resolution index[a]	40	40	50	55
GNSS satellites caught	6–8	6–8	6–9	8–11

[a] Spacing between laser shots on an artificial numeric scale designed by Optech™: the lower the value is, the higher the point cloud resolution will be

Table 3 Conditions and LiDAR parameters of acquisitions of the five scans realized on 25–26 September 2013

	M1′	M2′	J1′	J2′	J3′
Sector	St-Aubin>Dieppe	St-Aubin>Dieppe	Dieppe>Penly	Penly>Criel	Dieppe landslide
Scan beginning time	9h18	13h55	10h00	12h07	14h35
Scan end time	12h10	16h17	11h30	13h25	14h45
Acquisition length	15,700 m	16,900 m	9200 m	9450 m	600 m
Range to cliffs	600–800 m	~300 m	~600–800 m	~600–800 m	~300 m
Tide	Low	High	Low	Low	High
Boat velocity	~3.5–4.5 kn	~4 kn	~3.4 kn	~3.6 kn	~3.7 kn
Sea conditions (Beaufort)	1 Bft	1 Bft	2 Bft	3 Bft	2.5 Bft
Sun	From the side	Cloudy	From the side	Cloudy	Cloudy
LiDAR vertical aperture	20°	36°	22°	22°	36°
Angular resolution index[a]	45	55	45	45	55
GNSS satellites caught	6–8	9–12	6	8–10	9

[a] Spacing between laser shots on an artificial numeric scale designed by Optech™: the lower the value is, the higher the point cloud resolution will be
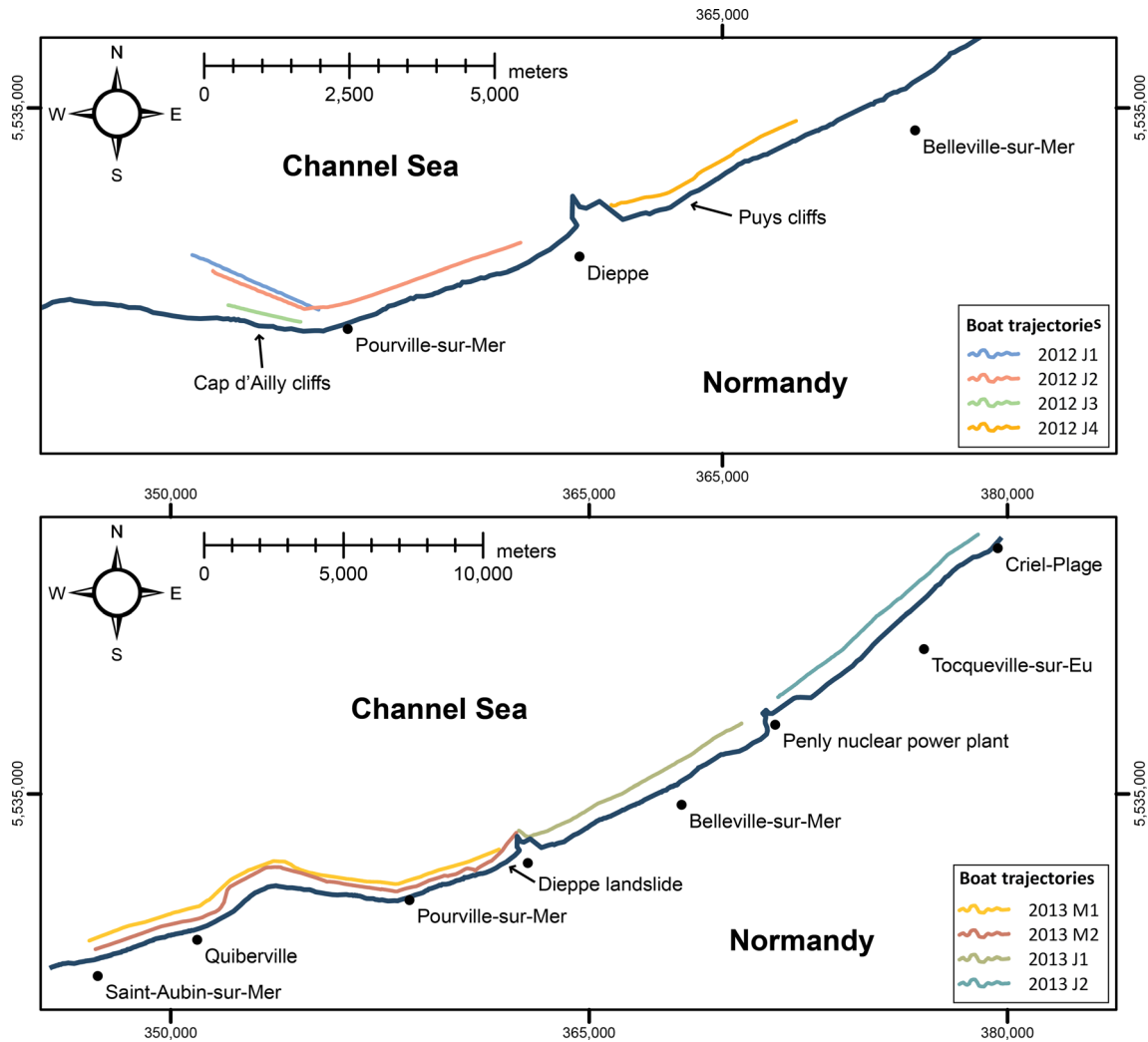
Fig. 4 Boat trajectories during acquisitions on 20 September 2012 of Cap d'Ailly and Puys cliffs (*up*) and on 25–26 September 2013 between Saint-Aubin-sur-Mer and Criel-Plage (*down*)
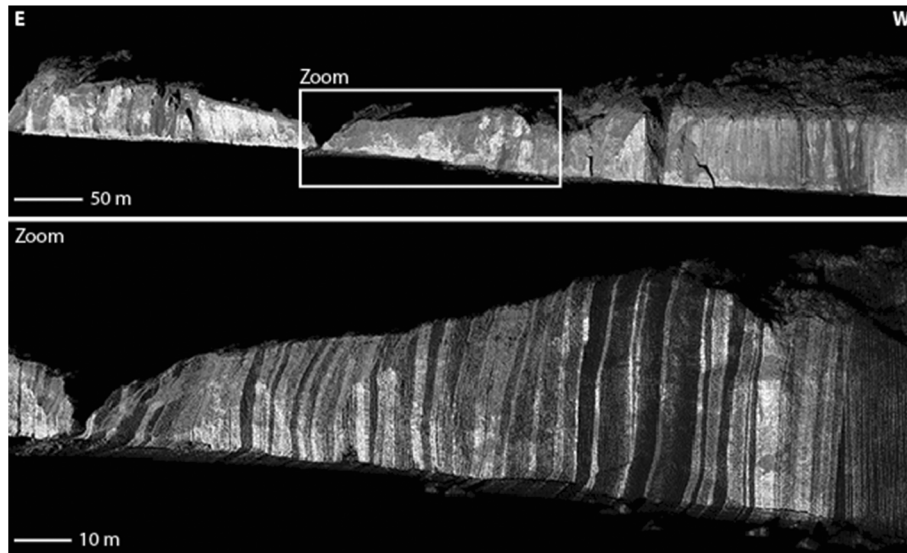
Fig. 5 *Up*: Final J3 point cloud of the Ailly site, manually and automatically cleaned, ready for the *xyzi* exportation; the cleaned scan has 3,118,836 points, instead of 3,234,761 initially (only 3.6 % of the points were deleted). *Down*: Zoom in the cliff sector that is long-term monitored with TLS acquisitions. Spacing between vertical lines is mainly varying with boat velocities when it is tossed by waves or it is surfing on them (cf. Fig. 7)

Encouraged by the 2012 experience, four acquisitions of about 10 km each, named Mn' and Jn', have been achieved on 25 and 26 September 2013 in similar conditions from Saint-Aubin-sur-Mer to Criel-Plage. A smaller point cloud focused on the active retrogressive Dieppe landslide (cf. "Rockfall detection and rock spread monitoring" section) has also been performed. Trajectories and conditions of acquisitions are illustrated in Fig. 4 and summarized in Tables 2 and 3.

Post-processing

Inertial navigation system data
INS-recorded data are first filtered by computing the smoothed best-estimated trajectories using the raw inertial and GNSS measurements. This correction, realized within the software Applanix POSPac™ MMS 5.3, indeed deletes outliers and artefacts from atmospheric perturbations and potential micro-losses of the GNSS signal.

Similarly to classic static GNSS studies (Gili et al. 2000), we then used close permanent GNSS antennas of the French Geographic Institute (IGN) as base stations to post-process and correct our GNSS signal. For the 2012 campaign, confined close to Dieppe, data from the Ambrumesnil permanent antenna has been used as base station. Regarding the 2013 campaign, for which acquisitions are covering 38 km of coast, GNSS data from several permanent antennas distributed along the coast were necessary for the post-processing: Ambrumesnil, Fécamp, Le Touquet, Cap Seine, Morgny, Houville-en-Vexin, Foucarmont and Herstmonceux permanent antennas. The final accuracy of post-processed positioning (trajectory and LiDAR LOS) is about 3 cm.

The INS navigation data are then projected in the UTM 31° N WGS 84 coordinate system and exported in the SBET and polyline shapefile formats, in order to be coupled with LiDAR data or imported within GIS software.
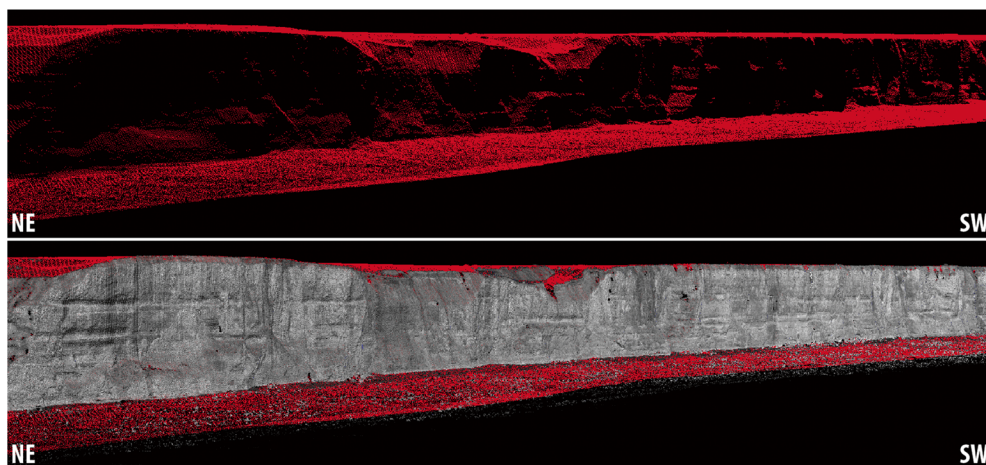

Fig. 6 Illustration of point density difference between the ALS point cloud ((*up*, *in red*) and the MLS point cloud (*down*, *in grey*) close to Puys (ALS data: © IGN)
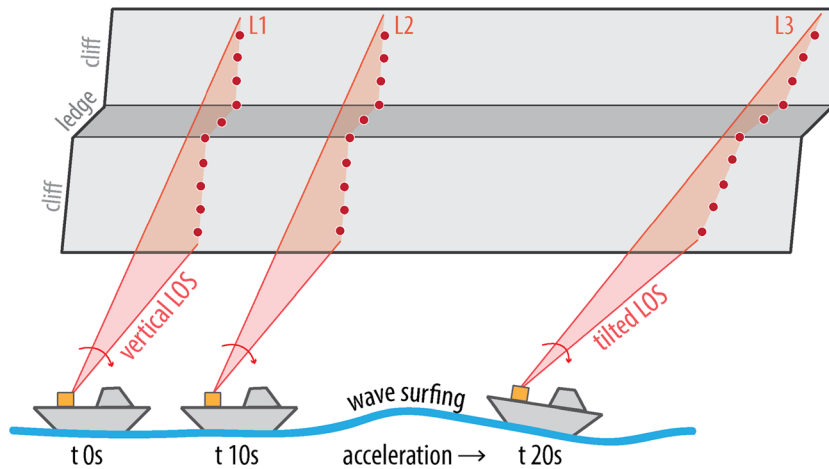
Fig. 7 Illustration of the influence of LiDAR setup and vessel attitude on the vertical and horizontal spacing. The horizontal spacing between L_1 and L_2 is lower than that between L_2 and L_3 since the boat accelerated when it surfed on a wave

Mobile laser scanning data

In order to get the final geometry of the LiDAR data, they have been processed according to the following procedure:

1. Raw LiDAR data, which are related to the LiDAR referential system, are coupled with positioning and orientation information of SBET files, synchronized together with GNSS time logs recorded on both files (the Raw and SBET ones).
2. Roto-translation matrices are then automatically computed and applied to each point using the software Optech™ Parser 5.0.3.1 in order to georeference the acquisition (in UTM 31° N WGS 84). Point clouds are exported in ASCII text files structured in four columns: coordinates x, y, z and intensity of the back-scattered signal (named hereafter *xyzi*).
3. Point clouds are then manually and iteratively cleaned, as for common post-processing of TLS data (Abellán et al. 2014): non-ground points, i.e. outliers from reflected pulses on sea spray and air dust, as well as direct sunshine misinterpreted as LiDAR signal, are manually selected based on a visual interpretation and are then deleted, within the software Polyworks™ PIFEdit 10.1.

4. After having carried out empirical and statistical analysis on signal intensities on representative populations of points reflected by sea spray, cliffs or sunshine, all points with signal intensity lower than 12 (on a scale [0;255]) have been considered as sea spray and foam and therefore deleted, within the software Polyworks™ ImInspect 10.1.
5. All cleaned point clouds are then re-exported in *xyzi* files (Figs. 5 and 6).
6. Subset areas containing only cliff areas and no vegetation or constructions are selected within 2012 and 2013 point clouds and are also exported in *xyzi* files.

The repeatability of MLS data is then assessed with only the 2012 acquisitions at the Cap d'Ailly (i.e. J1, J2 and J3, all acquired in an interval of 4 h):

7. The J1 and J3 point clouds are aligned on the J2 one, used as reference, by progressively minimizing the distances between points to the J2 meshed reference surface with an iterative closest point-based (ICP - Besl and McKay 1992) algorithm implemented in Polyworks™ ImInspect 10.1.

Table 4 Median and dispersion values of point spacing for each 2012 MLS acquisition

		J1	J2	J3	J4
Mean range and velocity		650 m/4 kn	450 m/4 kn	200 m/2.2 kn	300 m/3.3 kn
Aperture and resolution index		14°/40	14°/40	23°/50	18°/55
All points	Number of points	2,173,560	8,500,660	3,118,836	7,700,024
	Median spacing	22.7 cm	12.2 cm	8.0 cm	8.4 cm
	Quantile 68	15.5 cm	8.8 cm	4.9 cm	5.2 cm
	Quantile 95	42.9 cm	30.8 cm	16.6 cm	17.5 cm
Cliff subsets	Number of points	1,427,830	6,062,001	2,539,891	6,816,492
	Median spacing	20.5 cm	10.7 cm	7.6 cm	8.1 cm
	Quantile 68	13.8 cm	7.5 cm	4.5 cm	4.9 cm
	Quantile 95	33.7 cm	24.8 cm	15.1 cm	16.5 cm

Table 5 Median and dispersion values of point spacing for each 2013 MLS acquisition

	M1′	M2′	J1′	J2′	J3′
Mean range and velocity	700 m/4 kn	300 m/4 kn	700 m/3.4 kn	700 m/3.6 kn	300 m/3.7 kn
Aperture and resolution index	20°/45	36°/55	22°/45	22°/45	36°/55
Number of points	10,910,356	11,824,517	12,253,010	11,553,180	1,257,959
Median spacing	15.6 cm	14.0 cm	12.2 cm	14.2 cm	15.6 cm
Quantile 68	11.4 cm	10.5 cm	7.8 cm	8.0 cm	9.8 cm
Quantile 95	45.5 cm	36.2 cm	33.4 cm	33.0 cm	28.9 cm

8. The realigned point clouds are exported in *xyzi* files.

In order to assess the MLS capability to detect and monitor topographic changes due to rockfall events, erosions of former deposits and retrogressive landslides on the 2012 and 2013 sequential acquisitions:

9. The 2013 M2′ and J1′ point clouds are aligned on, respectively, the 2012 J2 and J4 ones, used as references, following the process described in step 6.
10. The realigned point clouds are exported in *xyzi* files.

As explained in the "Results" section, these alignments, which might seem useless since the point clouds are already georeferenced, actually enhance the comparison of sequential acquisitions by reducing errors from the navigation inaccuracies.

Terrestrial laser scanning point clouds

As a part of the wide researches conducted on the Dieppe coastline stability (Letortu 2013; Letortu et al. 2014), a long-term TLS monitoring is carried out on cliffs in Ailly and Puys. On 18–19 September 2012, TLS-based point clouds of both sites have been acquired with a Riegl LMS Z390i; the dataset, georeferenced in the UTM 31° N coordinate system using 16 ground control points (GCP), has a median point spacing of about 1 cm (cf. "Results" section). In order to compare scans from both techniques, the following procedure has thus been applied:

1. As a decametric vertical translation has been observed between TLS and MLS acquisitions, which may stem from different geoids used between French and Swiss partners,

the Ailly and Puys TLS point clouds are aligned on, resp., the J2 and J4 ones, used as references following the method described in step 6.
2. The TLS point cloud is exported in an *xyzi* file.

MLS point clouds capability assessment

Methodology

Median point spacing
The assessment of the resolution of each point cloud according to navigation conditions and device setup is described in this section. First, Euclidean distances of each point to its nearest neighbour have to be extracted. Then, statistics are achieved to describe the Euclidean distances distribution of each scan. For this purpose, the distribution median is first calculated; then, the 68 and 95 % quantiles of the difference to this median are computed to characterize the dispersion of the population. The median is preferred to the mean in order to minimize influences of outliers (Höhle and Höhle 2009). The process, implemented within a Matlab™ routine, follows these steps:

1. The cleaned *xyzi* point cloud is imported.
2. The *knnsearch* function (Friedman et al. 1977) is computed to search the nearest neighbour of each point and to then extract the Euclidean distance x between them.
3. The median $\bar{x}$ of all distances x is calculated.
4. For each point, the difference in absolute value $|x-\bar{x}|$ between the distance to its nearest neighbour and the median value is calculated.
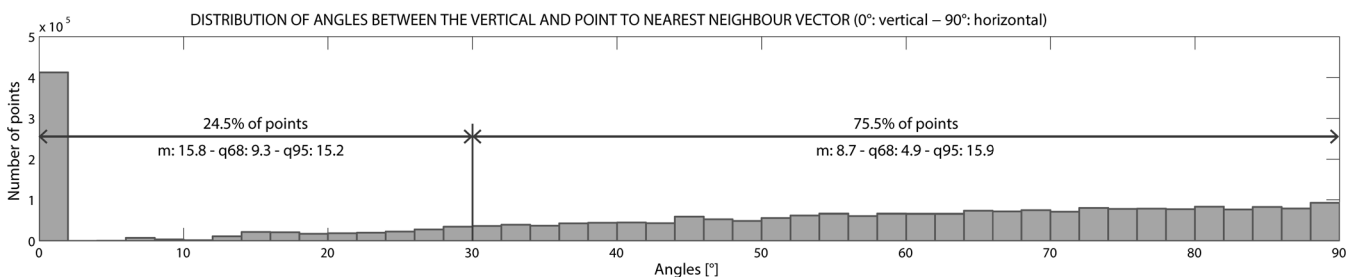5. The 68 and 95 % quantiles of the differences to the median are calculated.

DISTRIBUTION OF ANGLES BETWEEN THE VERTICAL AND POINT TO NEAREST NEIGHBOUR VECTOR (0°: vertical – 90°: horizontal)

24.5% of points
m: 15.8 - q68: 9.3 - q95: 15.2

75.5% of points
m: 8.7 - q68: 4.9 - q95: 15.9

Fig. 8 Angle distribution between the vertical and point-to-nearest neighbour vectors for the J3 subset point cloud: 24.5 % of the nearest neighbours are located on a vertical more or less 30° direction from points. Medians (*m*), 68 % (*q68*) and 95 % (*q95*) quantiles are in centimetres

Table 6 Median and dispersion values of point spacing for the two 2012 TLS acquisitions

	TLS Ailly	TLS Puys
Number of points	4,678,910	8,332,012
Median spacing	1.1 cm	0.6 cm
Quantile 68	4.6 cm	0.6 cm
Quantile 95	11.3 cm	10.8 cm

In addition, we aim at discriminating the influences on the cliff's point spacing of (a) the LiDAR device setup (especially its vertical aperture and angular resolution), which should have a strong vertical component since its internal mirror is set up in order to move the beam vertically only, and (b) the vessel attitude and its velocity, which should influence mostly the horizontal spacing (Fig. 7).

For this purpose, we apply to the J1, J3 and M1′ subset point clouds additional steps to sort the nearest neighbours in two classes, the nearest vertical and nearest horizontal ones:

6. Now, the 25 nearest neighbours to each point are identified, again based on the *knnsearch* function (Friedman et al. 1977).
7. The angles between a vertical vector and the point-to-neighbour vector are extracted from the dot products for each point to their 25 nearest neighbours:

    a. If the angles with the vertical are included within 0° and 30° (threshold arbitrary set to deal with small ledges and tilted LOS, cf. Fig. 7), neighbours are considered belonging

to the same LiDAR LOS and are therefore sorted with the nearest vertical neighbours class.

    b. If the angles with the vertical are included within 30° and 90°, neighbours are considered as not vertical and are therefore sorted with the nearest horizontal neighbours class (i.e. distances between LiDAR vertical LOS).

8. Again, statistics are achieved for the two classes, following the same procedure as before.

Acquisitions repeatability

According to technical specifications of devices (cf. "Devices' technical specifications" section), the vessel attitude and trajectories are acquired with precisions up to 0.01° and 2 cm, respectively. In addition, the LiDAR device records range measurements with a mean accuracy of 4 mm at 100 m. But in order to assess in real conditions the MLS repeatability capability, the J1, J2 and J3 point clouds are compared. As the Ailly cliffs are acquired the same day in 4 h, we assume that the scanned topography is the same for the three point clouds; differences between them stem hence from device measurement errors. The repeatability can then be quantified assessing the point cloud differences. J2 is thus used as a reference surface, having the best overlapping ratio between scans, and its comparison to J1 and J3 subsets is then assessed with the following procedure:

1. The *xyzi* J2 and J4 point clouds are imported in Polyworks™ ImInspect 10.1, and the reference surfaces are built according to a triangular mesh with a horizontal
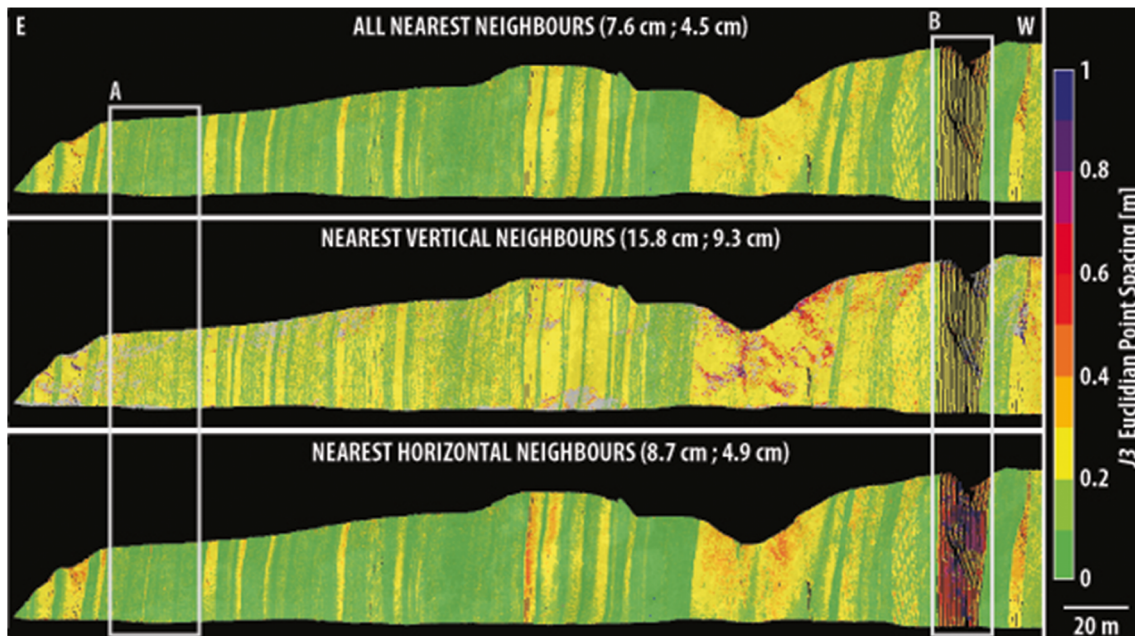

Fig. 9 Euclidean point spacing of the J3 subset point cloud considering all nearest neighbours (*up*), nearest vertical neighbours (*middle*) and nearest horizontal neighbours (*down*). *Frames A and B* match with examples developed in the text. *Numbers* in parentheses correspond to median and 68 % quantiles of point spacing distributions

Table 7 Median and dispersion values of shortest distances from J1 and J3 points to J2 meshed surface

	J2 (test)	Subset J1		Subset J3	
		Not aligned	Aligned	Not aligned	Aligned
Median spacing [cm]	12.2	20.5		8.1	
Median distance [cm]	0.0	0.0	0.0	−3.1	0.0
Median absolute distance [cm]	0.6	11.4	9.0	17.0	7.0
Quantile 68 [cm]	3.1	25.0	17.2	37.9	12.5
Quantile 95 [cm]	8.9	95.6	75.2	148.1	40.3

viewing vector (i.e. corresponding to a mean offshore position of the boat).

2. The aligned and not-aligned *xyzi* J1 and J3 subset point clouds (cf. "Mobile laser scanning data" section) are imported, as well as the realigned Ailly and Puys TLS point clouds (cf. "Terrestrial laser scanning point clouds" section).

3a. Based on the nearest-neighbour algorithm, the Euclidean shortest distances d from J1 to J3 points to the meshed reference surface J2 are computed.

3b. In the same way, the Euclidean shortest distances d from the TLS points of Ailly and Puys, respectively, to their meshed reference surfaces, J2 and J4, resp., are computed.

4. These distances d are also computed from J2 to J4 points to their own meshed surface, as tests to identify errors coming exclusively from the surface meshing step and not from instrumental ones.

5. All comparisons are exported in *xyzi* and d files.

Statistics on computed differences d are then carried out according to the same method as for point spacing characterization (cf. "Median point spacing" section), i.e. following a routine implemented in Matlab™:

6. The *xyzid* comparison files are imported.
7. The median $\overline{d}$ of all distances d is calculated.
8. The median $\overline{|d|}$ of all absolute distances $|d|$ is calculated.
9. For each point, the difference in absolute value $|d-\overline{d}|$ between the distance to its nearest neighbour is calculated.
10. The 68 and 95 % quantiles of the differences to the median $\overline{d}$ are calculated.

Change detection and monitoring

In order to detect topographic changes between the 2012 to 2013 acquisition campaigns due to rock slope failures, erosion of former deposits or retrogressive landslides, ICP-based distance comparisons between sequential dataset can be assessed in Polyworks™ ImInspect 10.1. Indeed, after having refined the alignment of new point clouds on old ones:

– Rockfall events are usually identified by computing shortest distances between the two topographies (Abellán et al. 2014).
– Retrogressive processes can easily be quantified by computing the horizontal distances parallel to the sliding direction (Jaboyedoff et al. 2009).

In addition, volumes of detected rockfall events can be estimated using an alpha-shape concave hull method (Edelsbrunner and Mücke 1994), following a semi-automatic routine shown in Carrea et al. (2014):

1. Each rockfall or erosion deposit identified with the shortest distance comparison has first to be delimited on both old and new surfaces.
2. Point clouds of rockfalls or deposit shapes are meshed with tetrahedrons in Matlab™ and:

   – Each tetrahedron basis contains no other point than the three ones of its edges.
   – Tetrahedron heights have to be big enough to allow the filling of the form, but in the meantime, small enough to avoid the filling of the block surface concavities.

3. For each identified block, the volume of the mesh is computed by summing the volume of all the tetrahedrons.

Table 8 Median and dispersion values of shortest distances from TLS points to J2 and J4 meshed surfaces

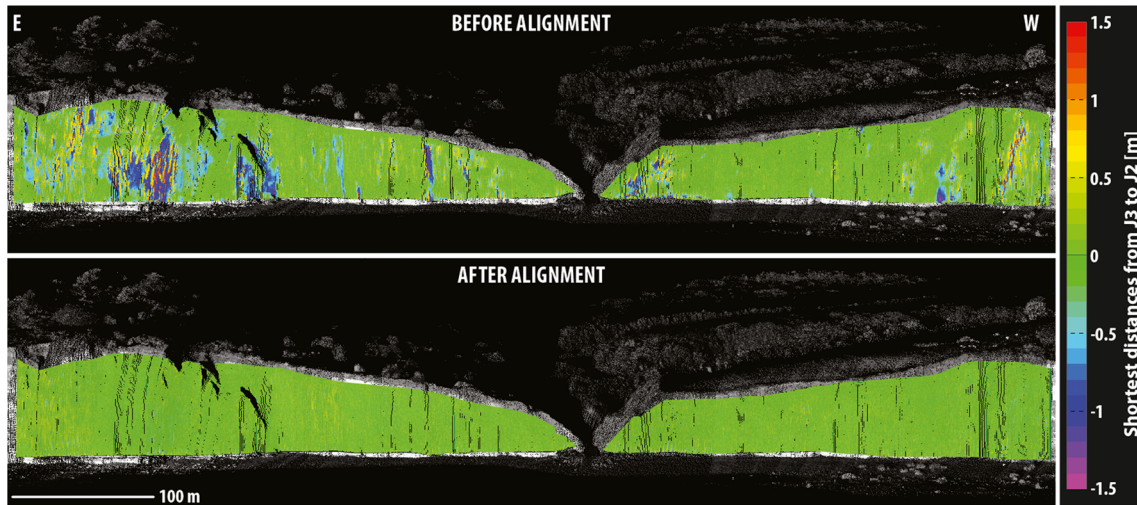|	Test J2	Test J4	TLS Ailly	TLS Puys
Aligned on	J2 (itself)	J4 (itself)	J2	J4
MLS median spacing [cm]	12.2	8.4	12.2	8.4
TLS median spacing [cm]	–	–	1.1	0.6
Median distance [cm]	0.0	0.0	0.0	0.0
Median absolute distance [cm]	0.6	1.1	4.7	4.2
Quantile 68 [cm]	3.1	0.1	7.8	7.1
Quantile 95 [cm]	8.9	6.3	27.7	31.9

Fig. 10 J3 points to J2 meshed surface Euclidean distances, before and after alignment (*positive values*: points in front of the reference surface; *negative values*: points behind the reference surface; *scale* in metres)

Results

Decimetric median point spacing

As summarized in Tables 4 and 5, median point spacing of scans ranges from 20 cm for far scans to about 8 cm for the closest ones. Acquired in low tide conditions in a range of 500 to 600 m and with a 4-kn stream (7.4 km/h), J1 and J2 have median point spacing of about 22 and 12 cm with 68 % quantiles of 16 and 9 cm. Acquired from 200 m and with a 2.2 kn stream (4.1 km/h), J3 has

a median point spacing of 8 cm with a 68 % quantile of 5 cm (Fig. 8). In addition, statistics on point spacing on subset clouds, focused on cliffs (our areas of interest), are almost equal to those of the complete scans because the majority of the points are located on these cliffs. As a comparison, the Ailly and Puys TLS-based point clouds have median point spacing of about 1 cm (Table 6).

Regarding the vertical and horizontal component of the J3 subset point spacing illustrated in Figs. 7 and 8, 24.5 % of points
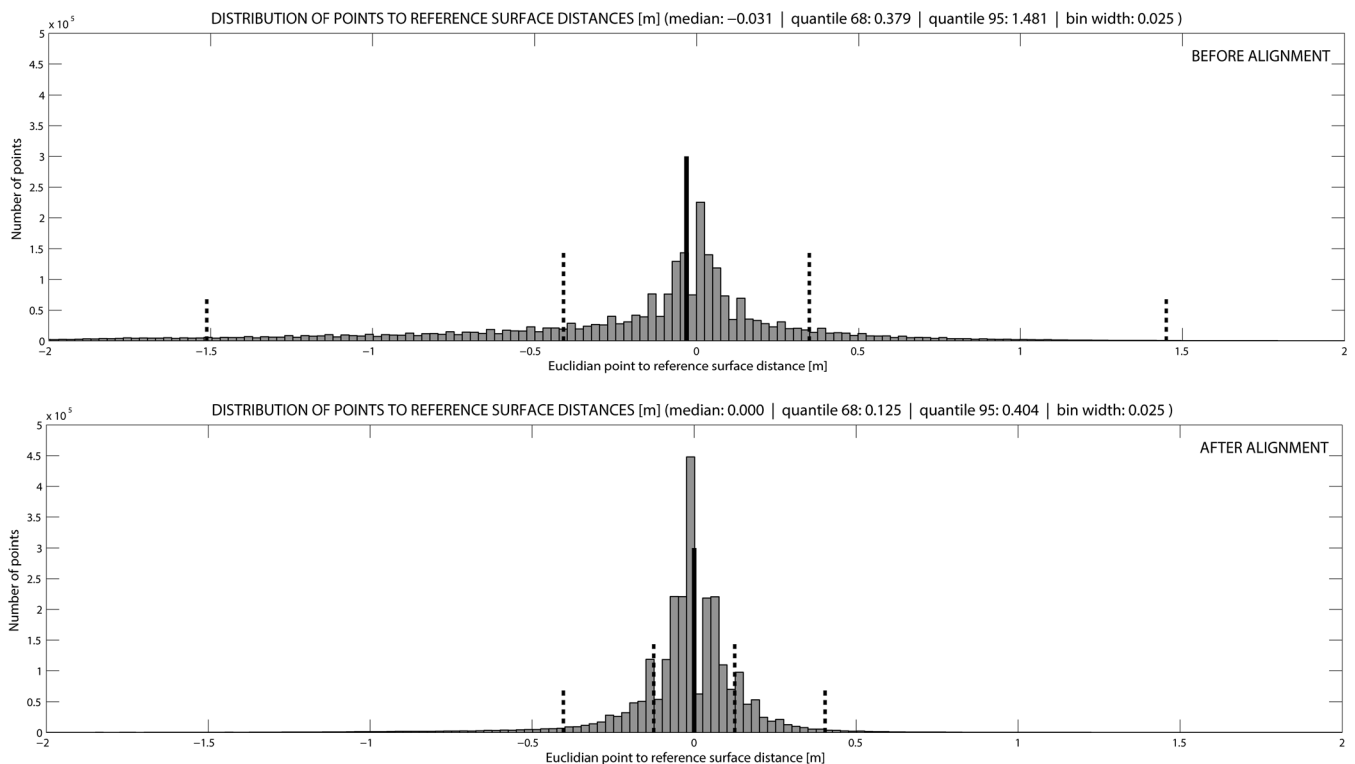
Fig. 11 Shortest distance distributions from J3 points to J2 meshed reference surface, before (*up*) and after (*down*) J3 alignment on J2 (*dark lines*: median; *dot lines*: 68 and 95 % quantiles)
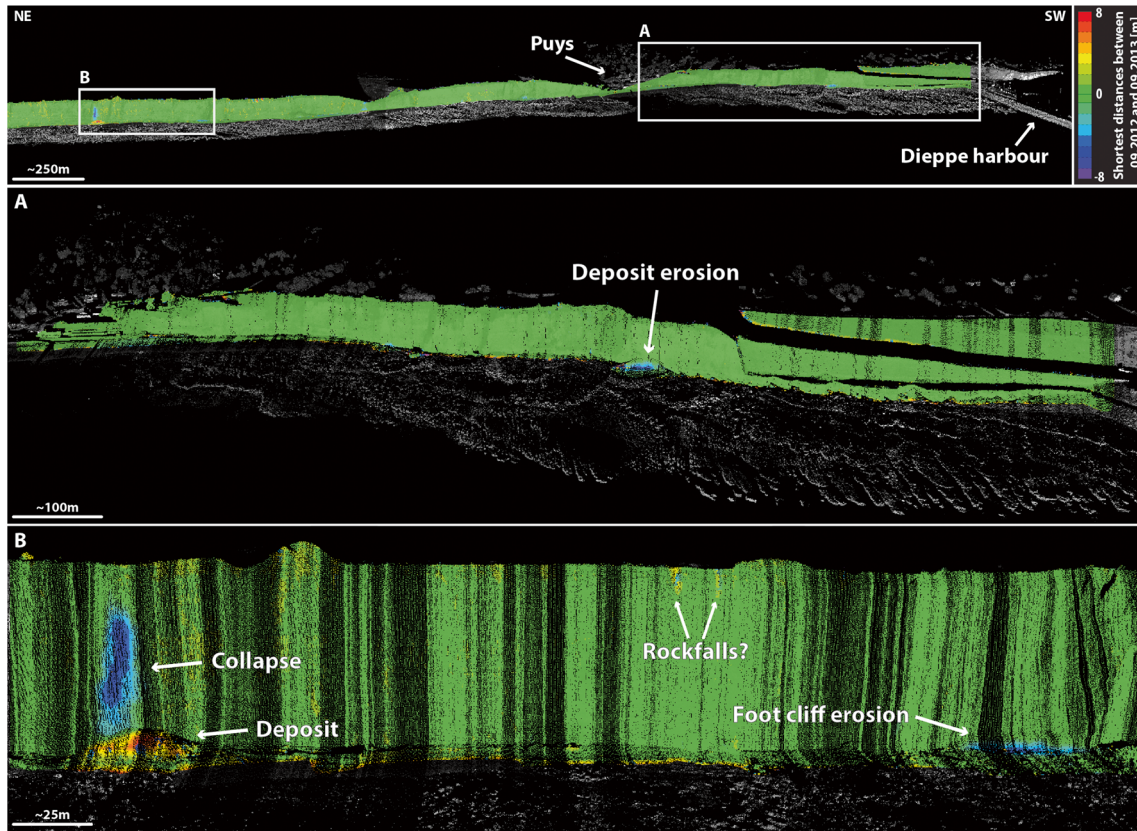
Fig. 12 Shortest J2′ points to J4 surface distances comparison between 2012 and 2013 point clouds wrapped on the intensities of the second scan. Only few collapses and deposit erosions are detected along the Puys shoreline and are detailed in the next caption. (*Negative values*: eroded material; *positives values*: accumulated material)

have their nearest neighbour close to the vertical, while 75.5 % of the points have it uniformly distributed on their side. In addition, when we compare distances to nearest vertical and horizontal neighbours, we notice that horizontal point spacing is usually lower than the vertical one (Fig. 9). It means that the vessel attitude, largely influenced by the boat velocity and marine conditions, is hence mainly controlling the general point spacing. Indeed, by navigating during a calm sea, the median horizontal point spacing is about 9 cm, while the median vertical one is about 16 cm (Fig. 9, frame A). On the contrary, when the boat is tossed and surfs on swells, the median horizontal point spacing can reach up to 58 cm, with a vertical one of about 24 cm (Fig. 9, frame B).

Finally, point cloud resolutions can be also improved independently of the navigation conditions, adapting the Optech™ device setup; for example, by setting in 2013 the LiDAR vertical aperture

at 20° and the angular resolution index at 45 (cf. Tables 2 and 3), instead of 14° and 40, the M1′ median vertical and horizontal point spacing (20 and 12 cm) are indeed much lower than the J1 ones (46 and 23 cm), although both were acquired in the same conditions (2 Bft), i.e. from 600 to 700 m with a 4-kn stream.

Decimetric repeatability after point cloud realignment
Now, regarding the MLS repeatability capability, comparison results between J1, J2 and J3 point clouds acquired in an interval of 4 h are summarized in Table 7. First, median absolute distances between points of the reference point clouds (J2) and its own triangulated mesh are lower than 1 cm, as expected, but with 68 and 95 % quantiles of about 3 and 9 cm; errors introduced during the surface meshing step, especially in vegetated areas, are likely to explain the observed differences of similar magnitude in the test.
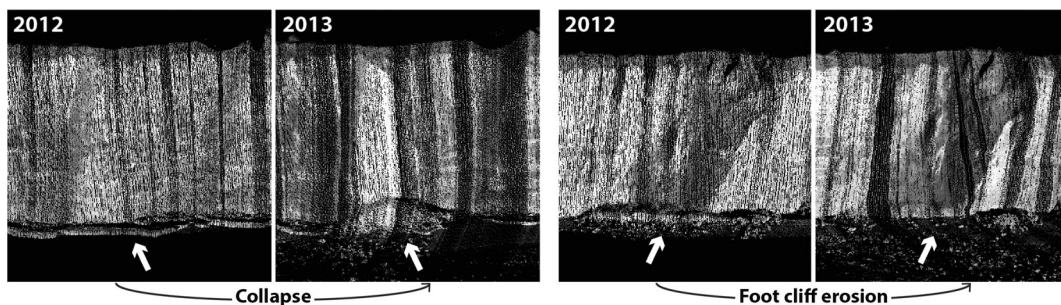

Fig. 13 Point cloud comparisons of the collapse and the foot cliff erosion highlighted in the previous figure
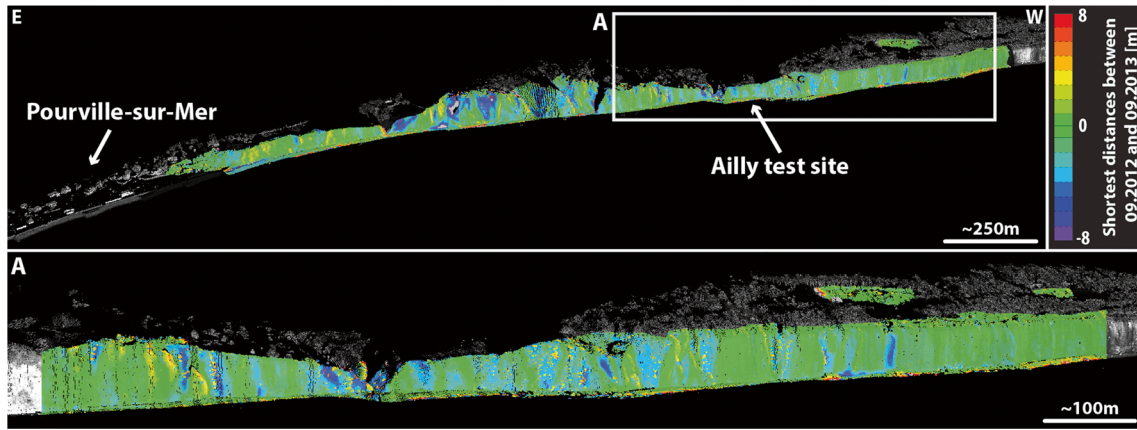
Fig. 14 Shortest M2′ points to J2 surface distances comparison between 2012 and 2013 point clouds wrapped on the intensities of the second scan. Multiple rockfall events can be easily identified and quantified close to the Cap d'Ailly. (*Negative values*: eroded material; *positives values*: accumulated material)

Then, the median of absolute distances between J1 and J3 points and the J2 reference surface are about 11 and 17 cm with 68 % quantiles of 25 and 38 cm. Nevertheless, once J1 and J3 are realigned on J2 (cf. "Mobile laser scanning data" section), both point clouds have smaller differences with the reference surface, the median of absolute distances decreasing to about 9 and 7 cm with 68 % quantiles of 17 and 12 cm. As a comparison, TLS acquisitions of Ailly and Puys sites are also realigned on J2 and J4 point clouds, resp., and compared with them (Table 8): the medians of absolute distances are close to 4 cm, with 68 % of 9 and 7 cm (resp.).

Differences between point clouds can therefore be drastically reduced by simply refining the alignment of all point clouds (Figs. 10 and 11), reinforcing the repeatability capability of the boat-based mobile scanning technique.

Rockfall detection and rock spread monitoring
Regarding the change detection capability, it is nowadays possible to quickly assess retreat rates over kilometre-long coastal cliffs. Our capability to detect, map and quantify in details rockfall events and cliff foot erosion between September 2012 and September 2013 is indeed confirmed with classic nearest-neighbours comparison approaches, as illustrated in Figs. 12, 13 and 14. We can furthermore notice a greater number of collapses along the Cap d'Ailly shoreline than the Puys one, as confirmed by geological and hydrogeological settings very prone to failure in complex cliffs of Ailly (Costa 2014).

We afterward estimated cliff retreat of the "Dieppe landslide": this large active sandy-clay earth and soft rock spread was activated on 17–18 December 2012 by the heavy autumnal and wintry rainfalls and destroyed several constructions (Fig. 15). By extracting horizontal differences approximately parallel to the sliding azimuth between the 2012 J2 and the 2013 J4′ point clouds, we measure a cliff retreat up to 40 m along two active scarps over 70 m wide (Figs. 16 and 17). Then, using the alpha-shape concave hull method (Edelsbrunner and Mücke 1994; Carrea et al. 2014), loss material volumes are estimated close to 100,000 m³, although the scree deposit volume is close to 35,000 m³, its major part being already eroded by the Channel waves and tidal currents.

Fig. 15 Dieppe landslide in September 2013 that destroyed several constructions close to the shoreline after its activation in December 2012
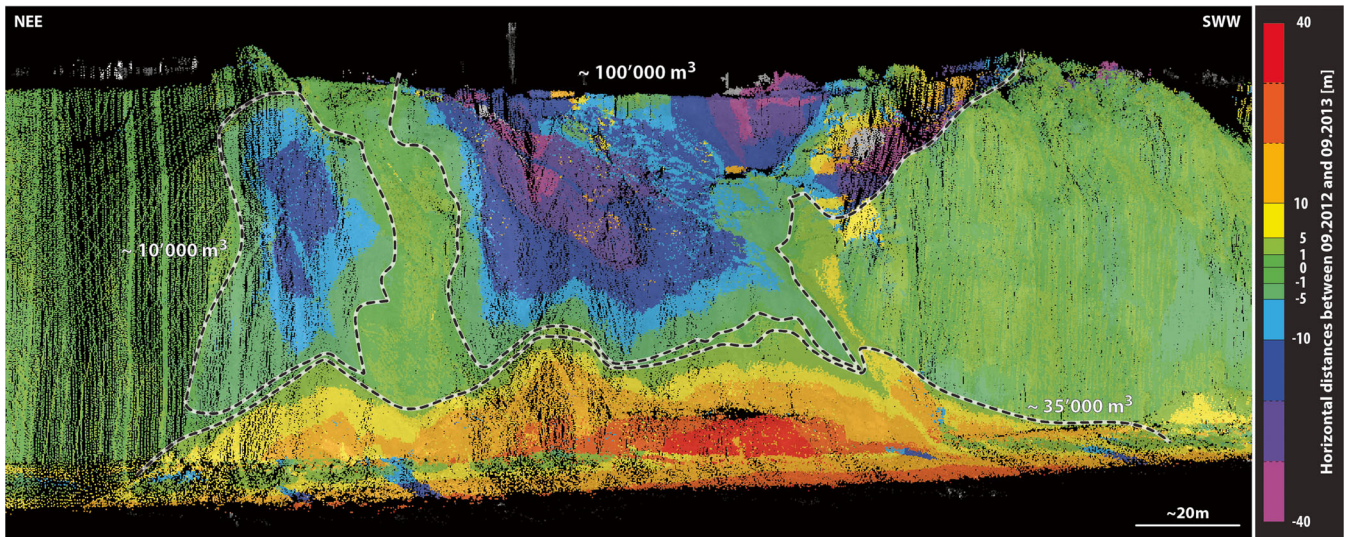
Fig. 16 Fine horizontal distances comparison parallel to the sliding direction between 2012 J22 and 2013 J4′ point clouds wrapped on the intensities of the second scan, on a large active retrogressive landslide that has been reactivated during spring 2013 and destroyed several constructions (*Negative values*: eroded material; *positives values*: accumulated material)

Discussion and conclusions

ALS devices have been widely used for coastal topography and shallow bathymetry modelling, especially with the SHOALS and derived systems (e.g. in Irish and Lillycrop 1999; Adams and Chandler 2002; Brock and Purkis 2009; Young et al. 2013; Earlie et al. 2014). But the incidence angle is a key factor for point cloud density and accuracy (Baltsavias 1999; Lichti et al. 2005). For coastal shore topography such as cliffs, ALS data have then high inaccuracy and lack of information on vertical areas due to unfavourable high incident angles (Adams and Chandler 2002; Young et al. 2013; Earlie et al. 2014). Meanwhile, boat-based MLS is a recent laser sensor development that is able to scan a kilometre-long sub-vertical coastline from a direct and horizontal point of view, improving point cloud densities and accuracies, and acquiring even overhangs. We here demonstrated along Dieppe coastal cliffs, High Normandy, France, that our MLS system (an Applanix POS MV INS coupled with an Optech Ilirs LR LiDAR), is indeed a promising technique supporting rockfall assessments and large landslide monitoring along vertical sea shores.

The navigation conditions, i.e. boat velocity and range to the cliffs largely controlling by Channel stream and tide, are mainly influencing the general point spacing; nevertheless, it can also be optimized with appropriate LiDAR device setup, in order to keep as coherent as possible vertical and horizontal spacing. First, by scanning during favourable meteorological and marine conditions (i.e. 2 Bft, very small swell and almost no stream, and no rain) and close to the coast (~200 m during high tide period), MLS devices are indeed able to quickly scan a long shoreline with a median point spacing up to 10 cm. For example, it took 1.5 h to scan 9 km of coastal cliffs at ~3.5 kn (6.5 km/h). Moreover, other tests performed during harsher conditions, with 1.5 m high swell and strong stream (4.5 Bft), also allowed us to extract 3D data with point spacing of about 30 cm. Nevertheless, scanning during quiet days is a better guarantee for a dense and uniform cover of areas of interest since the LiDAR LOS is more easily controlled when the boat is not continuously tossed by waves.

Then, by increasing the laser pulse repetition frequency of newer LiDAR devices, point cloud resolution can also be
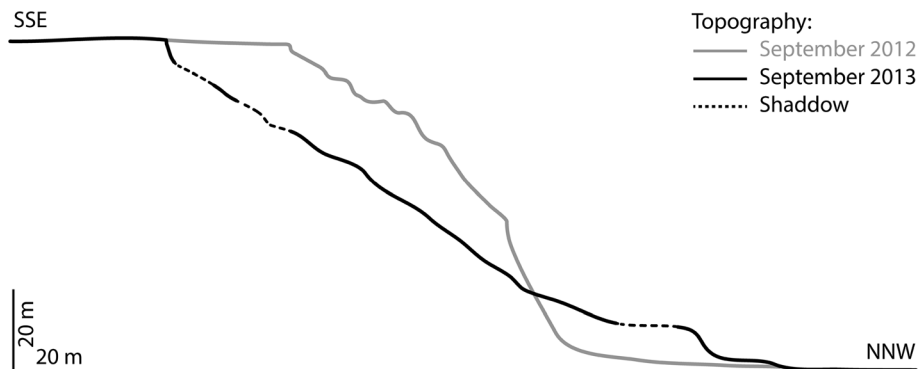

Fig. 17 Topography prior to and after the "Dieppe" landslide, extracted from September 2012 and September 2013 MLS acquisition coupled with the ALS data at the flat top

enhanced. Indeed, previous acquisitions performed in Norwegian fjords and carried out with equivalent navigation conditions, but with an Ilris TLS of older generation with a pulse rate four times lower of 2.5 kH, produced point clouds with median spacing of about 50 cm (Michoud et al. 2010).

In addition, the monitoring with MLS of the constant erosion with millimetre and centimetre rates seems up to now not realistic, with measured repeatability close to 10 cm. Nevertheless, more accurate LiDAR, based on phase shift between emitted and received signals instead of TOF principles (Vosselman and Maas 2010), can have repeatability of about 1 cm (e.g. in Vaaja et al. 2013). However, these devices cannot perform scans from ranges longer than 150 m, strongly limiting their capabilities in areas with long intertidal zones, where boats do not navigate, such as in Dieppe. Nevertheless, precisions of our data are sufficient to map geomorphological features smaller than 0.5 m^2 along coastal cliffs.

At the same time, our capability to detect rockfalls and erosion deposits (>m^3) is confirmed with classic approaches computing shortest distances between sequential acquisitions. Sectors with different rockfall susceptibilities have indeed been underlined, clearly detecting many cliff collapses between Pourville and Quiberville and only sparse changes between Dieppe and Belleville-sur-Mer. In addition, the Dieppe large landslide geometry has also been described, emphasizing two main active scarps with retrogression up to 40 m and about 100,000 m^3 of eroded materials. In order to enhance detection mapping, we suggest dividing the point clouds in shoreline sections of constant aspect to refine alignments of piecewise data on the interpolated mesh of the reference point cloud; this alignment step actually minimize uncertainties from the INS measures.

Finally at larger scales, ALS and MLS might thus be used as complementary techniques along long coastlines with successions of gentler and steeper topographies more adapted to resp. ALS and MLS devices. Additional acquisitions should be performed in the North of the study area along gentler slopes to experiment the potential inputs of using both techniques. Meanwhile, MLS capabilities for accurate change detection and mass balance monitoring along sub-vertical coastlines at low costs (compared to ALS devices and flights) could really support:

- Cliff retreat rates assessments for different sectors, by automatically extracting surfaces affected by rockfalls, compared to the entire surface of kilometre-long scanned cliffs. The routine developed by Carrea et al. (2014), which computes volumes, is indeed already able to individualize each collapsed block and could hence be adapted to also assess their surfaces.
- Landslide modelling and forecasting (Fukuzono 1990; Leroueil 2001; Rosser et al. 2007; Abellán et al. 2010; Royán et al. 2014) to manage risks dealing with affected infrastructures and inhabitants.

References

Abellán A, Calvet J, Vilaplana JM, Blanchard J (2010) Detection and spatial prediction of rockfalls by means of terrestrial laser scanner monitoring. Geomorphology 119:162–171

Abellán A, Oppikofer T, Jaboyedoff M, Rosser NJ, Lim M, Lato MJ (2014) Terrestrial laser scanning of rock slope instabilities. Earth Surf Process Landf 39:80–97

Adams JC, Chandler JH (2002) Evaluation of LiDAR and medium scale photogrammetry for detecting soft-cliffs coastal change. Photogramm Rec 17:405–418

Alho P, Kukko A, Hyyppä H, Kaartinen H, Hyyppä J, Jaakkola A (2009) Application of boat-based laser scanning for river survey. Earth Surf Process Landf 34:1831–1838

Applanix Corporation (2011) POS MV V5 installation and operation guide, revision 3

Baltsavias EP (1999) Airborne laser scanning: basic relations and formulas. ISPRS J Photogramm Remote Sens 54:199–214

Baroň I, Supper R (2013) Application and reliability of techniques for landslide site investigation, monitoring and early warning—outcomes from a questionnaire study. Nat Hazards Earth Syst Sci 13:3157–3168

Beraldin JA, Blais F, Boulanger P (2000) Real world modelling through high resolution digital 3D imaging of objects and structures. ISPRS J PhotogramM Remote Sens 55:230–250

Besl PJ, McKay ND (1992) A method for registration of 3D shapes. IEEE Trans Pattern Anal Mach Intell 14:239–256

Brock JC, Purkis SJ (2009) The emerging role of lidar remote sensing in coastal research and resource management. J Coast Res SI(53):1–5

Carrea D, Abellán A, Derron MH, Jaboyedoff M (2014) Automatic rockfalls volume estimation based on terrestrial laser scanning data. In: Proceedings of the IAEG XII Congress, 15–19 September 2014, Turin Italy, 6 p

Collins B, Sitar N (2008) Processes of coastal bluff erosion in weakly lithified sands, Pacifica, California, USA. Geomorphology 97:483–501

Costa S (1997) Dynamique littorale et risques naturels: L'impact des aménagements, des variations du niveau marin et des modifications climatiques entre la Baie de Seine et la Baie de Somme. PhD thesis of the University of Paris I (Panthéon Sorbonne), 347 p

Costa S (2014) The High Normandy chalk cliffs: an inspiring geomorphosite for painters and novelists. In: Fort M, André MF (eds) Landscapes and landforms of France. Springer, New York, pp 29–39

Costa S, Delahaye D, Freiré-Diaz S, Davidson R, Di-Nocera L, Plessis E (2004) Quantification by photogrammetric analysis of the Normandy and Picardy rocky coast dynamic (Normandy, France). In: Mortimore RN, Duperret A (eds) Coastal chalk cliff instability. Engineering Geology Special Publications, Geological Society, London, pp 139–148

Dewez T, Rohmer J, Regard V, Cnudde C (2013) Probabilistic coastal cliff collapse hazard from repeated terrestrial laser surveys: case study from Mesnil Val (Normandy, northern France). J Coast Res 65:702–707

Duperret A, Genter A, Mortimores RN, Delacourt B, De Pomerai MR (2002) Coastal rock cliff erosion by collapse at puys, France: the role of impervious marl seams within chalk of NW Europe. J Coast Res 18:52–61

Earlie CS, Masselink G, Russell PE, Shail RK (2014) Application of airborne LiDAR to investigate rates of recession in rocky coast environments. J Coast Conserv 15 p

Edelsbrunner H, Mücke EP (1994) Three-dimensional alpha shapes. ACM Trans Graph 13:43–72

Friedman JH, Bentely J, Finkel RA (1977) An algorithm for finding best matches in logarithmic expected time. ACM Trans Math Softw 3:209–226

Fukuzono T (1990) Recent studies on time prediction of slope failure. Landslide News 4:9–12

Gili J, Corominas J, Rius J (2000) Using global positioning system techniques in landslide monitoring. Eng Geol 55:167–192

Glennie C, Brooks B, Ericksen T, Hauser D, Hudnut K, Foster J, Avery J (2013) Compact multipurpose mobile laser scanning system—initial tests and results. Remote Sens 5:521–538

Gordon S, Litchi D, Stewart M (2001) Application of a high-resolution, ground-based laser scanner for deformation measurements. In: Proceedings of the 10th International Symposium on Deformation Measurements, 19–22 March 2001; Orange USA, 23–32

Höhle J, Höhle M (2009) Accuracy assessment of digital elevation models by means of robust statistical methods. ISPRS J Photogramm Remote Sens 64:398–406

Irish JL, Lillycrop WJ (1999) Scanning laser mapping of the coastal zone: the SHOALS system. ISPRS J Photogramm Remote Sens 54:123–129

Jaakkola A, Hyyppä J, Hyyppä H, Kukko A (2008) Retrieval algorithms for road surface modelling using laser-based mobile mapping. Sensors 8:5238–5249

Jaboyedoff M, Demers D, Locat J, Locat A, Locat P, Oppikofer T, Robitaille D, Turmel D (2009) Use of terrestrial laser scanning for the characterization of retrogressive landslides in sensitive clay and rotational landslides in river banks. Can Geotech J 46:1379–1390

Jaboyedoff M, Oppikofer T, Abellán A, Derron MH, Loye A, Metzger R, Pedrazzini A (2012) Use of LIDAR in landslide investigations: a review. Nat Hazards 61:5–28

Kukko A, Kaartinen H, Hyyppä J, Chen Y (2012) Multiplatform mobile laser scanning: usability and performance. Sensors 12:11712–11733

Leroueil S (2001) Natural slopes and cuts: movement and failure mechanisms. Geotechnique 51(3):197–243

Letortu P (2013) Le recul des falaises crayeuses haut-normandes et les inondations par la mer en Manche centrale et orientale: de la quantification de l'aléa à la caractérisation des risques induits. PhD thesis of the University of Caen Basse-Normandie 414 p

Letortu P, Costa S, Cantat O (2012) Les submersions marines en Manche Orientale: approche inductive et naturaliste pour la characterisation des facteurs responsables des inondations par la mer. Climatologie 9:31–57

Letortu P, Costa S, Bensaid A, Cador JM, Quénol H (2014) Vitesses et rythmes de recul des falaises crayeuses de Haute-Normandie (France). Géomorphol Relief Process Environ 2:133–144

Lichti D, Gordon S, Stewart M (2002) Ground-based laser scanners: operation, systems and applications. Geomatica 56:21–33

Lichti D, Gordon S, Tipdecho T (2005) Error models and propagation in directly georeferenced terrestrial laser scanner networks. J Surv Eng 131:135–142

Lim M, Petley DN, Rosser NJ, Allison RJ, Long AJ, Pybus D (2005) Combined digital photogrammetry and time-of-flight laser scanning for monitoring cliff evolution. Photogramm Rec 20:109–129

Michoud C, Longchamp C, Derron MH, Jaboyedoff M, Blikra LH, Kristensen L, Oppikofer T (2010) The terrestrial and offshore laser scanning acquisitions of September 2010 in Sunndalsøra (Møre og Romsdal, Norway)—techniques, processing and data. Internal technical report University of Lausanne, Lausanne 10 p

Michoud C, Bazin S, Blikra LH, Derron MH, Jaboyedoff M (2013) Experiences from site-specific landslide early warning systems. Nat Hazards Earth Syst Sci 13:2659–2673

Oppikofer T, Jaboyedoff M, Blikra LH, Derron MH, Metzger R (2009) Characterization and monitoring of the Åknes rockslide using terrestrial laser scanning. Nat Hazards Earth Syst Sci 9:1003–1019

Rosser NJ, Petley DN, Lim M, Dunning SA, Allison RJ (2005) Terrestrial laser scanning for monitoring the process of hard rock coastal cliff erosion. Q J Eng Geol Hydrogeol 38:363–375

Rosser NJ, Lim N, Petley DN, Dunning S, Allison RJ (2007) Patterns of precursory rockfall prior to slope failure. J Geophys Res 112:F04014

Royán MJ, Abellán A, Jaboyedoff M, Vilaplana JM, Calvet J (2014) Spatio-temporal analysis of rockfall pre-failure deformation using terrestrial LiDAR. Landslides 11:697–709

SafeLand deliverable 4.1 (2012) Review of techniques for landslide detection, fast characterization, rapid mapping and long-term monitoring. Michoud C., Abellán A., Derron M.-H. and Jaboyedoff M. (eds.), SafeLand European project, 401 p., available at http://www.safeland-fp7.eu

Tupling SJ, Pierrynowski MR (1987) Use of cardan angles to locate rigid bodies in three-dimensional space. Med Biol Eng Comput 25(5):527–532

Vaaja M, Hyyppä J, Kukko A, Kaartinen H, Hyyppä H, Alho P (2011) Mapping topography changes and elevation accuracies using a mobile laser scanner. Remote Sens 3:587–600

Vaaja M, Kukko A, Kaartinen H, Kurkela M, Kasvi E, Flener C, Hyyppä H, Hyyppä J, Järvelä J, Alho P (2013) Data processing and quality evaluation of a boat-based mobile laser scanning system. Sensors 13:12497–12515

Vosselman G, Maas H (2010) Airborne and terrestrial laser scanning. CRC Press, Boca Raton

Williams K, Olsen MJ, Roe GV, Glennie C (2013) Synthesis of transportation applications of mobile LiDAR. Remote Sens 5:4652–4692

Young AP, Olsen MJ, Driscoll N, Flick RE, Gutierrez R, Guza RT, Johnstone E, Kuester F (2013) Comparison of airborne and terrestrial LiDAR estimates of seacliff erosion in southern California. Photogramm Eng Remote Sens 76:421–427

C. Michoud · D. Carrea · M.-. Derron · M. Jaboyedoff
Institute of Earth Sciences,
University of Lausanne,
Lausanne, Switzerland

S. Costa · O. Maquaire · P. Letortu · R. Davidson
LETG-CAEN GEOPHEN,
Universit de Caen Basse-Normandie,
Caen, France

C. Delacourt
LDO, UMR 6538,
Université de Bretagne Occidentale,
Brest, France

C. Michoud (✉)
Terr@num,
35bis rue de l'industrie, Bussigny, Switzerland
e-mail: clement.michoud@terranum.ch